Textured Manganite Films Anywhere

Alexis Boileau, Marie Dallocchio, Florent Baudouin, Adrian David, U. Luders, Bernard Mercey, Alain Pautrat, Valérie Demange, Maryline Guilloux-Viry, Wilfrid Prellier, et al.

Textured Manganite Films Anywhere

Alexis Boileau[1§], Marie Dallocchio[1§], Florent Baudouin[2], Adrian David[1], Ulrike Lüders[1], Bernard Mercey[1], Alain Pautrat[1], Valérie Demange[2], Maryline Guilloux-Viry[2], Wilfrid Prellier[1], Arnaud Fouchet[1]*

1 NORMANDIE UNIV, ENSICAEN, UNICAEN, CNRS, CRISMAT, 14000 CAEN, France

2 ISCR, Univ Rennes, CNRS, ISCR – UMR 6226, ScanMAT – UMS 2001, F-35000 Rennes, France

* Corresponding author:
E-mail: arnaud.fouchet@ensicaen.fr

§: A.B and M.D contributed equally to this work

Keywords: LSMO thin films, nanosheets, electrical properties, magnetic properties, glass substrate

Abstract:

New paradigms are required in microelectronic when the transistor is in its downscaling limit and integration of materials presenting functional properties not available in classical silicon is one of the promising alternatives. Here, we demonstrate the possibility to grow $La_{0.67}Sr_{0.33}MnO_3$ (LSMO) functional materials on amorphous substrate with properties close to films grown on single crystalline substrate by use of a two-dimensional seed layer. X-ray diffraction and electron backscatter diffraction mapping demonstrate that $Ca_2Nb_3O_{10}^-$ nanosheets (NS) layer induces epitaxial stabilization of LSMO films with a strong out-of-plane (001) texture, whereas the growth of LSMO films on uncoated glass substrates exhibit a non-textured polycrystalline phase. Magnetic properties of LSMO films deposited on NS are similar to those of the LSMO grown on $SrTiO_3$ single crystal substrates in the same conditions (which is used as reference in this work). Moreover, transport measurements take advantages of the texture and polycrystalline properties in order to induce low field magnetoresistance at low temperature and also a high value of 40%

magnetoresistance from 10 to 300 K interesting for sensor applications. Therefore, NS seed layer offers new perspectives for the integration of functional materials grown at moderate temperature on any substrate which will be the key for the development of oxitronics.

1. Introduction

In the near future, new materials will be required beyond the mainly used CMOS (Complementary Metal Oxide Semiconductor)-based electronics with new and dramatically improved properties, providing innovative paradigms for information storage and data processing (More-than-Moore approach)[1,2]. Complex oxides are potential candidates thanks to their exceptionally broad range of versatile functionalities, a number of them being not present in classical semi-conductors. Among these oxides, the doped $La_{0.67}Sr_{0.33}MnO_3$ manganite (LSMO) is a reference material for its remarkable electronic and magnetic properties[3–5]. The magnetic diagram of LSMO system has a large variety of phases depending on the composition with outstanding magnetic and transport properties[6,7]. LSMO has the largest single electron bandwidth and the highest Curie temperature (T_C) among the perovskite manganites, making it an interesting material for application in spintronic devices[8]. The strontium content leads to hole doping of the manganite, controlling the charge density at the Fermi level. Notably, LSMO exhibits a colossal magnetoresistance (CMR) and a ferromagnetic-metallic state (FM-M) at room temperature with high T_C of 369 K for a substitution rate of ~30% for La, rendering this oxide very interesting for applications as sensor[9,10], in spintronics[11–14] and for magneto-optical and optoelectronic applications[15,16]. Moreover, LSMO exhibits a low resistivity at high temperature and can be used as an electrode in solid oxide fuel cells-based devices[17,18]. Also, its integration on flexible substrates (mica, polymers…) represents of utmost interest for emerging applications in spintronics or electronics in bending conditions[8]. Nevertheless, the magnetic and transport properties of LSMO can be tuned by various factors, such as external hydrostatic pressure[19], oxygen stoichiometry[20,21], Sr doping level[22], as well as the strain effect[23] because of the sensitive lattice-spin-charge coupling. For example, epitaxial LSMO films exhibits lower T_C than polycrystalline films of about 20 K[24,25]. In this way, it may be possible to tune magnetic and transport properties of films by inducing a texture or near-epitaxy of LSMO films on non-adapted substrates. However, the coexistence of optimized properties and its integration onto

low cost substrates as silicon for the electronics industry or amorphous materials as glass is a current challenge required to overcome technological limitations. Indeed, growth of LSMO directly on silicon is extremely complicated due to the incompatibility between their respective crystalline structure and their reactivity with oxygen. This issue leads to very low crystalline quality of LSMO thin films together with a large degradation of their properties. This is due to the high reactivity of unsaturated silicon bonds at the surface of the substrate leading to an oxidation of the surface and the formation of a SiO_2 layer. Even at low deposition temperatures, this layer cannot be avoided, and may lead to problems regarding the epitaxial growth[26,27].

The main approach to circumvent these difficulties was the integration of high quality functional oxides as LSMO films on Si with the growth of a buffer layer by using for example TiN, CeO_2/Y_2O_3, $SrTiO_3$ (STO) and more recently $SrRuO_3$/TiN, by molecular beam epitaxy or pulsed laser deposition[28–34]. Nevertheless, the process is generally tedious and not adapted to large-scale production due to its complexity and high temperature process. Moreover, this method requires necessarily the use of a crystalline substrate and cannot be transferred easily to larger lattice mismatched or amorphous substrates as a-Si or SiO_2, for example. Therefore, regarding the use of complex oxides in a large scale, new approaches are a necessary prerequisite for the integration of complex oxides.

Another approach for complex oxides integration onto non-adapted substrates is the use of nanosheets (NS) as seed layer[35]. In this approach, NS created by an exfoliation process of layered oxides are transferred on low cost large-surface substrates as silicon or glass, providing the seed layer for the growth of complex oxide thin films independently on the bottom substrate material. These NS can be synthesized from precursors prepared by solid state route, followed by an exchange reaction of protonation in solution and finally exfoliation to obtain the colloidal dispersion suitable to transfer the NS on the substrate by Langmuir-Blodgett method[36]. These NS are exceptionally rich in structural diversity (cubic, rectangular, hexagonal structures…) and can be used as seed layers to induce epitaxy of a wide range of complex oxides. A large variety of layered oxides are dedicated to the perovskite structures. The NS obtained by exfoliation of layered structures such as Ruddlesden-Popper phases (for instance $SrLaTi_2TaO_{10}^{2-}$ and $Ca_2Ta_2TiO_{10}^{2-}$), Dion-Jacobson phases (for instance $(Ca,Sr)_2(Nb,Ta)_3O_{10}^-$ and $LaNb_2O_7^-$)and Aurivillius phases (for instance $(Sr,Bi)Ta_2O_7^{2-}$ and $Bi_4Ti_3O_{12}^{2-}$) [37] open new perspectives for the integration of oxides onto non-adapted substrates. Among the NS obtained from these layered oxides, $Ca_2Nb_3O_{10}^-$ (CNO) has been

used for the growth of various materials as TiO_2 [38], $CaBi_4Ti_4O_{15}$ [39], or $(Na_{1-x}K_x)NbO_3$ [40], $SrTiO_3$ [41] and $SrRuO_3$ [35,42]. The Dion-Jacobson parent phase $KCa_2Nb_3O_{10}$ crystallized in the monoclinic system (a = 0.7741 nm, b = 0.7707 nm, c = 1.4859 nm, β = 97.51°, JCPDS card N°01-075-9853) and is usually described in a larger tetragonal unit cell with lattice constants a = 0.7727 nm and b = 2.9466 nm[43,44]. Its structure consists in stacking of slabs of 3 perovskite layers laying in the (001) plane, separated by a cation (K^+) layer. After exfoliation, the two-dimensional lattice of the nanosheets has a square a-b plane with a_{NS} = 0.384 nm. Therefore, the use of CNO NS as seed layer is especially well-adapted for the growth of $La_{0.67}Sr_{0.33}MnO_3$ with a lattice parameter of 0.386 nm in the pseudo-cubic description, leading to a misfit of only -0.18 %. Moreover, CNO NS layer exhibits a good thermal stability. It has been reported to be stable up to 800°C in air[37], and segregates into a mixture of $Ca_2Nb_2O_7$ and $CaNb_2O_6$ above this temperature. Similarly, Kweon *et al.* report that the thermal stability of CNO NS is ensured up to ~600°C, depending on the number of layers[40]. Thus CNO NS layer is expected to be suitable for the growth of epitaxial LSMO films by pulsed laser deposition since, in our deposition system, the optimal temperature was around 640°C on single crystals $SrTiO_3$ substrates[25,45], in a partial pressure of oxygen.

In this paper, we report the structural and physical properties of highly (001)-textured LSMO films deposited on CNO NS seed layer using glass as substrate (GS). The local epitaxy of LSMO resulting from the growth of the film on small crystalline domains formed by the juxtaposition of the buffer CNO NS offers the possibility to investigate the electronic and magnetic properties of textured film on amorphous substrate. The properties of these textured film were compared with those of polycrystalline[46] and fully strained films[25,40], using not covered glass and STO substrates, respectively. Furthermore, the influence of the growth temperature on the different type of substrates was also investigated in order to demonstrate the potential of NS for the growth of LSMO at intermediate temperature.

2. Experimental Section

First, powder of $KCa_2Nb_3O_{10}$ oxide was synthesised by solid state reaction. Precursors oxides K_2CO_3 (Acros Organics, 99 %), Ca_2CO_3 (R.P. Normapur, 99.5 %) and Nb_2O_5 (Alfa Aesar, 99.5 %) were ball-milled in ethanol during 5 h before a thermal treatment at 1100°C during 10 h. Following Ebina *et al.*'s method[47], the $KCa_2Nb_3O_{10}$ oxide was then proton-

exchanged in 6 M HNO_3 for 3 days. The protonated phase was exfoliated by reaction with tetra(n-butyl)ammonium hydroxide (TBAOH) in a molar ratio 1:1, during 14 days. The obtained $TBACa_2Nb_3O_{10}$ nanosheets (NS) were deposited on fused silica substrates (glass substrate (GS): 10 × 10 × 0.5 mm, Neyco, NEGS3) by Langmuir-Blodgett method with the help of a KSV NIMA instrument. After that, deposited NS/GS samples were subjected to a thermal treatment at 110°C during 90 min followed by an exposition to UV radiations during 45 min to enhance the adhesion of NS on GS and remove adsorbed residual solvents. TEM characterizations of the NS are presented on Figure S1.

Then, $La_{0.67}Sr_{0.33}MnO_3$ (LSMO) thin films have been grown on cut 5 × 5 × 0.5 mm^3 NS/GS prepared samples, pristine GS and (001)-oriented $SrTiO_3$ (STO) substrates by pulsed laser deposition (PLD). Prior to deposition of LSMO, GS and STO substrates were successively cleaned in acetone and ethanol ultrasonic baths. A KrF excimer laser (λ= 248 nm) was used with a repetition rate of 2 Hz and a laser fluence adjusted to get a deposition rate close to 0.1 Å per laser pulse. This beam laser is focused on a $La_{0.67}Sr_{0.33}MnO_3$ polycrystalline target prepared by standard solid-state reaction. The deposition was carried out under oxygen ozone mixture[25]. The deposition pressure at the growth temperature was 5 × 10^{-4} mbar. The LSMO thickness was fixed to be around 40 nm for all samples by adjusting the deposition time. In order to investigate the influence of the temperature on the crystallization of LSMO films, the substrate temperature (T_G) was set at 550°C and 645°C. A 40 nm thick LSMO film grown on (001)-oriented STO in similar conditions sample was taken as reference throughout this work (see Figures S3 and S4). All thicknesses have been confirmed using X-ray reflectometry (see Figure S6).

The structural properties were characterized by X-ray diffraction (XRD) with a Philips X'Pert MRD diffractometer operating with monochromatic Cu $K_{\alpha 1}$ radiation (λ = 1.5406 Å) and equipped with a Pixel detector. The morphology of films was investigated by scanning electron microscopy (SEM) with a Zeiss Supra 55 (FEG source) and atomic force microscopy (AFM) Pico SPM-LE of Molecular Imaging in tapping mode. The surface coverage of glass substrates by NS is estimated around 90% by AFM imaging acquired on different large scale areas of the samples (see Figure S2 (d)). In order to get better insight of the structural dependence between LSMO and NS deposited glass, electron backscatter diffraction (EBSD) mapping of sample surfaces were performed on the SEM microscope equipped with a ultra-sensitive high resolution detector from Bruker at an accelerating voltage of 15 kV. Data are

computed by means of Esprit Software. The phase identification and orientations of LSMO/GS and LSMO/NS/GS samples are based on imposed starting structural references in the computational method. The rhombohedral and hexagonal structure descriptions of LSMO have been defined for the two respective samples.

The magnetization of LSMO films was determined using a Squid MPMS XL Quantum Design. The sample was placed in the sample holder with a parallel configuration to the magnetic field H. The calculated error is ~ 22 emu.cm^{-3}. This error takes into account the measurement errors of the magnetization (Squid device error: $\Delta m = 5 \times 10^{-6}$ emu), the surface of square samples determined by direct measurement ($\Delta L = 3 \times 10^{-5}$ m) and the thickness determined by X-Ray reflectometry ($\Delta t = 1 \times 10^{-9}$ m). The main error originates from the surface measurements of the sample. The temperature dependence of transport properties was determined by the four probe method from 5 K to 370 K in a physical properties measurement system (PPMS) by Quantum Design. The magnetoresistance was determined at 300 K and 5 K by applying successively a magnetic field of 0 and 9 T perpendicular to the film surface.

3. Results and discussion

3.1. Structural analyses

Scanning electron microscopy (SEM) micrographs of LSMO films deposited on GS and NS/GS samples are displayed in Figure S7. For uncoated GS samples, the deposition of LSMO leads to a flat and homogenous surface over the entire sample surface, independently of the growth temperature (T_G). In contrast, SEM micrographs taken on GS samples coated by NS show a tessellated surface due to the juxtaposition of NS. The size of the NS in an equiaxed-shape description is between 100 nm to 2 µm for the largest ones. The darker areas between well-delimited nanosheets are related to LSMO deposited on not covered glass zones. An analysis of the images provides a surface coverage level of the substrate with NS close to 90% (see Figure S2 (d)).

To get better insight of the morphology of LSMO films, Atomic Force Microscopy (AFM) characterizations are displayed in Figure S8 and Figure 1 for 10 × 10 µm² area and a zoom of 2 × 2 µm² area, respectively. For the NS/GS samples, the NS are juxtaposed

alongside each other even if small overlapping is revealed in some places. As it is observed above by SEM analyses, AFM images confirm the excellent coverage level of the surface by NS.

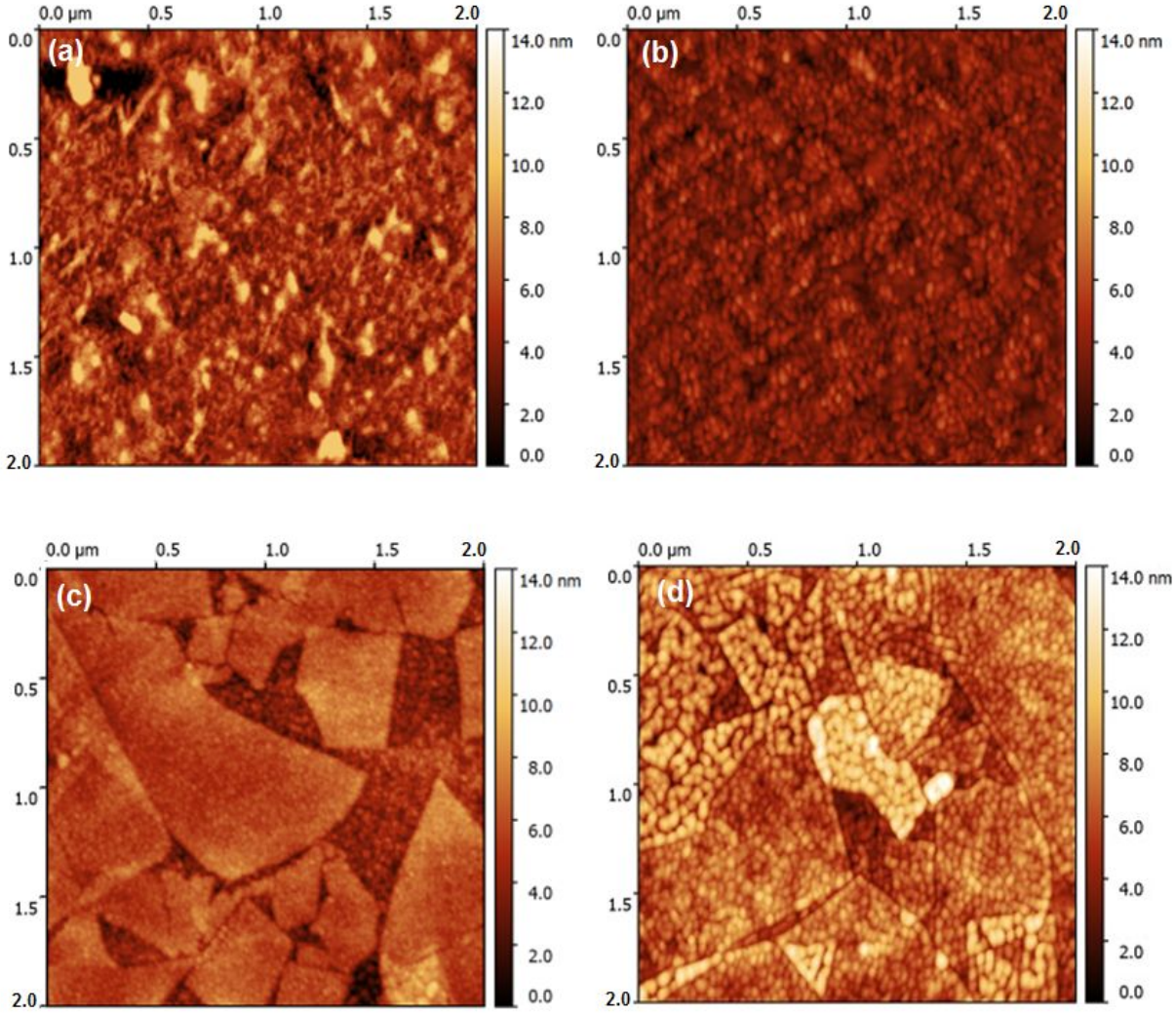

Figure 1. 2 × 2 µm² AFM images of LSMO films grown on GS (a-b) and NS/GS (c-d) at 550°C and 645 °C respectively. A granular structure of films appears at high deposition temperature.

However, important differences are observed in the morphology of films as function of the substrate and the growth temperature (T_G). Without NS, the surface is uniform and exhibits an apparent roughness due to the presence of long-tipped streaks ascribed to the glass substrate. The root mean square (RMS) roughness increases from 0.35 nm up to 0.70 nm for

growth temperature at 550 and 645°C, respectively. For the NS coated glass substrates, the films cover the NS and the interstices. The RMS roughness increases from 0.20 up to 0.47 nm when T_G rises from 550°C up to 645°C. Interestingly, small domains identified by a granular morphology are discernible (Figure 1 (d)). The estimation of the average particle size with the rise of T_G gives an increase from ~20 to ~40 nm for LSMO/GS samples and 20 to 50 nm for LSMO/NS/GS samples. The swelling of grains is correlated to the apparent roughness of films determined above and the T_G increase. The roughness of LSMO films is considerably lower than the values (between 14 and 56 nm) reported by Nguyen et al.[48] for 2 μm-thick columnar $Pb(Zr_{0.52}Ti_{0.48})O_3$ films grown on $LaNiO_3$/CNO nanosheets. In our case, the growth of LSMO films carried out with a lower repetition rate of the laser and growth rate (2 Hz and 0.1 Å per pulse, respectively) and significantly lower thickness (40 nm) lead to lower surface roughness.

The structural characterizations of LSMO films have been carried out by X-ray diffraction in specular θ-2θ configuration. The corresponding diffractograms at different T_G are shown in Figure 2. First, LSMO films grown directly on amorphous glass substrate exhibit a polycrystalline structure indexed according to the rhombohedral structure (space group $R\bar{3}c$) known to be the structure of LSMO deposited by pulsed laser deposition or by sputtering magnetron onto non-adapted substrates[46,49]. According to the required energy for the crystallization of films, a significant increase in the crystallinity is observed between 550 and 645°C due to a higher thermal activation. The lattice parameters, hexagonal setting, are found to be a = 0.550(2), c =1.337(8) nm and a = 0.546(7) nm, c = 1.331(8) nm for T_G = 550°C and 645°C, respectively. These values are in good agreement with data reported by Hibble *et al.* for bulk rhombohedral LSMO[50]. In the absence of an adapted template layer provided by CNO NS, the growth temperature is sufficient to induce the spontaneous crystallization of LSMO in the rhombohedral structure identified as the structure of the bulk material with a complete relaxation of intrinsic strains. For LSMO films deposited on NS/GS, a strong increase in the intensity related to the (001), (002) and (003) reflections (pseudo-cubic setting) is observed which means that the presence of the CNO NS induces a texturation of LSMO on NS with a 00l out-of-plane direction as for the LSMO film grown on single crystal (001)STO substrate. The out-of-plane lattice parameter of the LSMO phase is found to be close to 0.384(5) nm (550°C) and 0.383(6) nm (645°C) (pseudo-cubic setting). It can be mentioned that no reflection related to the NS layer is evidenced in XRD scans because of the too small diffraction volume. Nevertheless, the values of LSMO films match closely with CNO

reported in the literature [38,43,44,51], thereby confirming the epitaxial stabilization of the LSMO cell on the CNO one. A slight increase in the peak intensity is observed between 550 and 645°C indicating that the crystalline quality is enhanced with the increase of T_G. Finally, for LSMO grown on (001)STO, the out-of-plane lattice parameters determined from the high resolution θ-2θ scans (Figure S4) are c = 0.383(8) and 0.385(2) nm at 550 and 645°C, respectively which are very close to the values observed for the films deposited on NS. For LSMO films grown on GS, NS/GS and STO substrates at 645°C, full width at half maximum (FWHM) values obtained from the rocking curves of the (002) peak (not shown here) are 2.85, 1.33 and 0.04°, respectively. Hence, the mosaicity of LSMO films is dependent on the nature of the substrate with an enhancement of the structural quality of films grown on glass thanks to the NS seed layer.

The average size of the crystallite domains was determined using the Scherrer's formula[52]. The size increases with T_G from 14 to 34 nm and from 21 to 40 nm for LSMO/GS samples and LSMO/NS/GS, respectively. These values match closely with the ones of granular domains determined above in enlarged AFM scans (see Figure 1). Therefore, the increase of T_G as well as the use of NS enhances the size of crystallite domains and the structural quality of films. For LSMO deposited on GS, the thermal energy promotes the diffusion of adatoms on the surface resulting in the increase of the grain size. For LSMO grown on NS/GS, a similar behavior is observed as function of T_G but grains are larger than on GS showing that diffusion of the add-atoms seems more important on NS than on only GS.

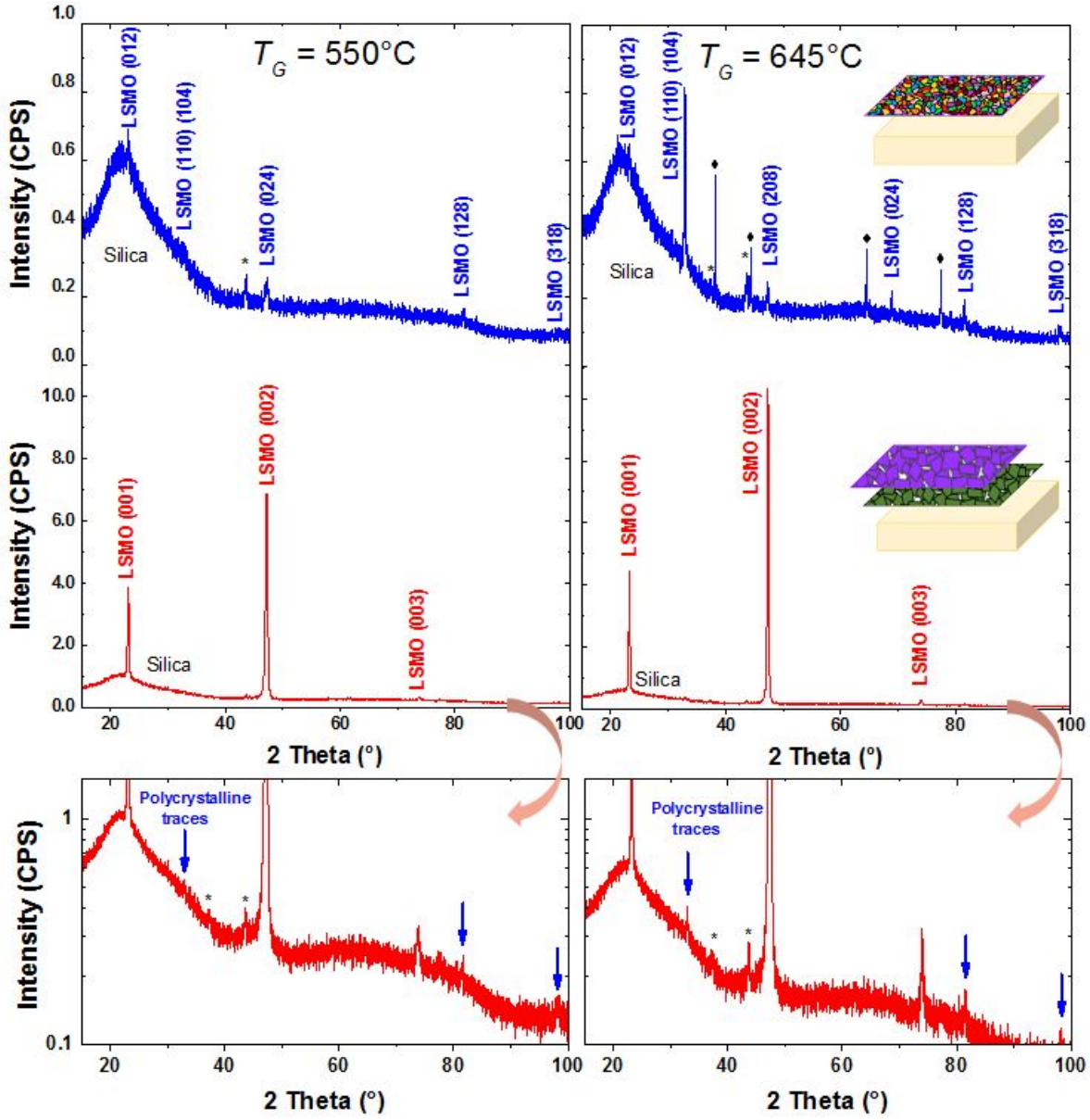

Figure 2. *θ-2θ* X-ray diffractograms of LSMO thin films grown on GS (blue) and NS/GS substrates (red) at 550°C and 645°C. Zoom in diffractograms of LSMO/NS/GS films reveal peaks attributed to the polycrystalline phase. Stars (*) and diamond (♦) symbols refer to instrumental artefact and silver traces, respectively.

In order to study the texture of the film in more details, electron backscatter diffraction (EBSD) mapping is reported in Figure 3 for LSMO films deposited onto NS/GS at 550°C (a and b) and 645°C (c and d) for out-of-plane and in-plane configuration, respectively. The mapping of the surface highlights the tessellated areas similar to SEM imaging (see Figure S7) corresponding to the size of the NS. All the electron backscattered beam signal is considered to be assigned to the LSMO film since the thickness of NS is too small to be detected. LSMO films are showing a preferential orientation along the [001] direction as seen

with the standard stereographic triangle (see Figure 3). The texturation is induced by the NS crystalline structure and confirms our previous XRD measurements. In-plane analysis reported in Figure 3 (b) and d reveals a mixed contribution between the [100] and [110] crystallographic directions of the LSMO and confirms the full disorientation of in-plane domains. Furthermore, some areas also appear in black and can be ascribed to areas being not covered by NS (see Figure S7 and S8). To understand this phenomenon, EBSD mapping was also performed on polycrystalline LSMO films deposited on GS (not shown here). Unfortunately, the polycrystalline domains size seems to be too small and do not allow a sufficient diffracting volume to be indexed in the limit of resolution of our device and appears black. Considering this along with the spontaneous crystallization of LSMO on GS, the areas between NS seems to be covered by polycrystalline LSMO. The observation in XRD scans of additional reflections at 32.8°, 81.5° and 98.2° on LSMO films deposited on NS/GS substrates (red enlarged scans in Figure 2) supports the EBSD observations. These additional reflections can be attributed to the rhombohedral phase but their low intensity indicates that the corresponding diffraction volume is small and could arise from the interstitial gaps between NS. In other words, NS induce LSMO epitaxial growth along the out-of-plane direction but does not induce the texture around the NS. For that reason, it is important to reach a high coverage level of the GS surface by NS. The orientation of LSMO on NS does not seem to depend strongly on the growth temperature but actually on the presence or absence of NS.

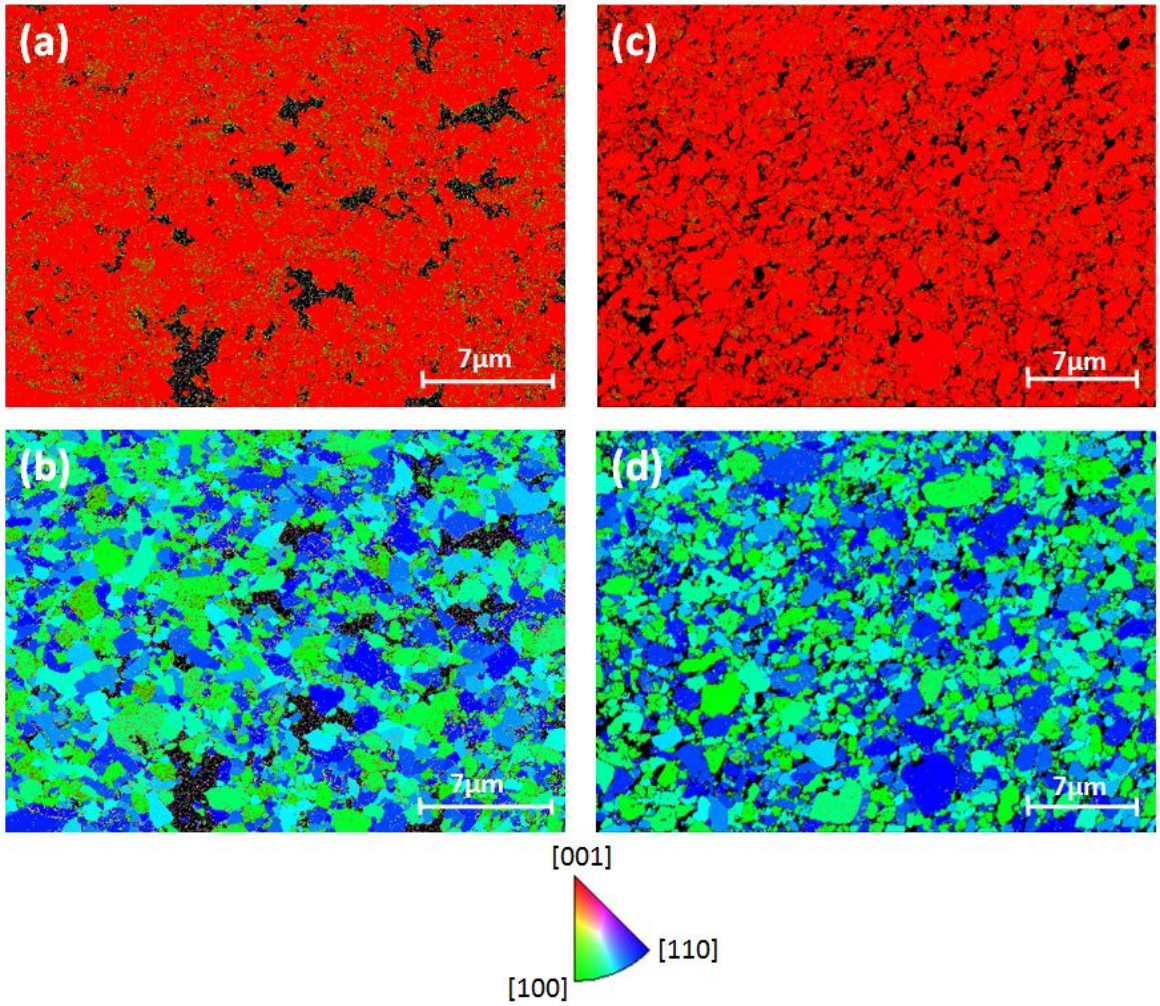

Figure 3. EBSD maps of LSMO thin films deposited at 550°C (left panel) and 645°C (right panel) on glass substrates coated by NS, (a, c) out-of-plane and (b, d) in-plane configuration. The out-of-plane images single-red color demonstrate that LSMO films are highly textured along the [001] direction.

3.2. Magnetism

The temperature dependence of the magnetization (M) of LSMO films is shown in Figure 4 (a) and (b) for films grown at T_G = 550°C and 645°C, respectively. A magnetic field of 0.05 T is applied parallel to the film surface. Two LSMO/STO samples grown at 550°C and 645°C in similar conditions than on GS and NS/GS are taken as references to compare the magnetic properties. For all the curves, the magnetization increases below T_c around 300 K to reach a plateau in the low temperature range (below ~150 K) but some differences are observed both in the amplitude of the magnetization and T_c of films.

Interestingly, the magnetization of LSMO/NS/GS films approaches closely the single crystal films for both T_G. At the contrary, a difference of M of around 170 emu cm^{-3} is observed between the films grown on GS and the buffered NS film for both T_G (all data are reported in Table 1). Furthermore, for LSMO grown directly on GS, M tends to slightly increase with T_G of about 15 emu.cm^{-3} (from 256 up to 271 emu.cm^{-3}) but remains substantially lower than values of LSMO films on NS/GS and STO due to the polycrystalline structure of the films. The same trend is observed for films deposited on NS/GS with a rising of M up of 18 emu.cm^{-3} (425 (550°C) to 443 emu.cm^{-3} (645°C)). By comparison, the magnetization of LSMO/STO samples tends also to increase from 453 and 463 emu.cm^{-3} with the T_G raising. These results are consistent with values reported in references[25,45,53] for LSMO/STO thin films above the critical LSMO thickness of about 10 nm for which magnetic and electrical properties are altered. In this regard, the growth temperature does not affect critically the magnetization and can be related to the improvement of the crystallinity with T_G.

In order to accurately measure the Curie temperature (T_C) of the films by the derivative method (see Figure S9), the $M(T)$ was measured with a magnetic field of 0.005 T around the magnetic transition after applying a field of 1 T at low temperature (see inset Figure 4 (a) and (b)). For LSMO films grown directly on GS at 550 and 645°C, they exhibit a T_C equal to 333 and 348 K, respectively. These values are somewhat greater than LSMO grown on a single STO crystal where a sharp magnetic transition occurs around T_C of 304 and 332 K for increasing T_G. Therefore, the T_C measured for LSMO/GS films is very consistent with data reported by Navasery *et al.*[49] in the case of polycrystalline LSMO. For LSMO on STO, the LSMO film is clamped on the crystalline substrate. The induced tensile strain driven by the lattice mismatch between the substrate and the film (-1.15%) leads to a deformation of the perovskite structure accompanied by a tilting of the O–Mn–O bonds and a diminution of T_C compared to the bulk[54,55]. In contrast, the crystallization of LSMO deposited on GS leads to polycrystalline structure with the complete relaxation of strains which explains the displacement of T_C close to the bulk LSMO one (T_C is within the range between 360 and 370 K). For textured LSMO films deposited on NS, the T_C found at 318 K and 337 K at 550°C and 645°C, respectively, is between the values measured for LSMO films deposited on GS and on (001)STO because of the combined contribution of both polycrystalline structure and local epitaxy on NS.

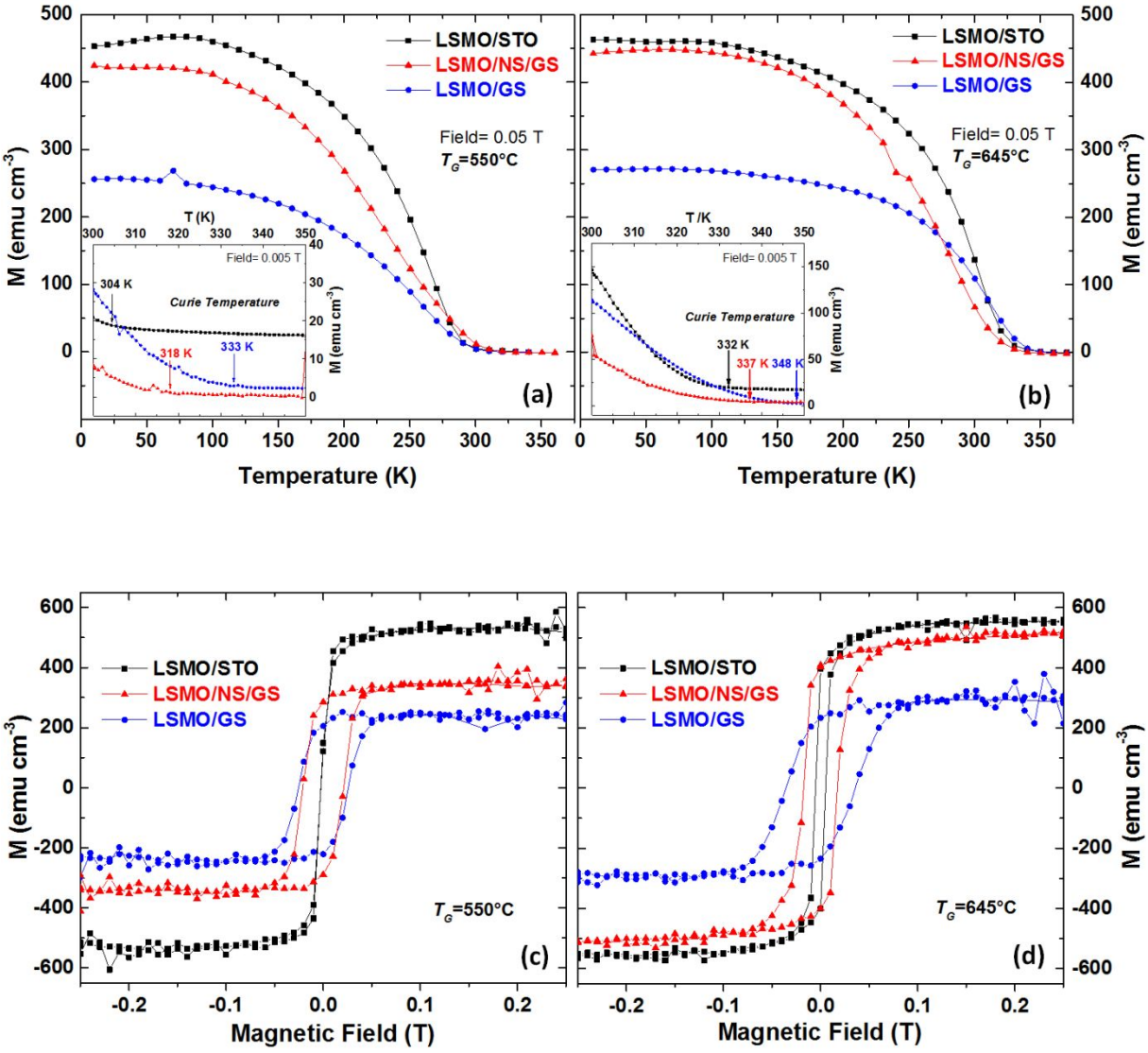

Figure 4. Temperature-dependent magnetization curves of LSMO films grown at 550°C (a) and 645°C (b) on GS (blue), NS/GS (green) and (001)STO (black). A magnetic field of 0.05 T and 0.005 T (in insert) was applied parallel to the surface for all the zero field cooled. Hysteresis loops acquired at 100 K of LSMO thin films grown at 550°C (c) and 645°C (d) for GS, NS cover GS and (001)STO substrates.

The hysteresis loops displayed in Figure 4 (c) and (d) are acquired at 100 K, just below the decrease of the magnetization (~150 K). Overall, the variation of the magnetization is consistent with the temperature-dependent magnetization curves described above. The remanent magnetic field B_R and the saturation magnetic field B_{Sat} gradually increase for LSMO films deposited on GS, NS/GS and STO substrates, respectively (see values summarized in Table 1). The influence of the growth temperature on B_{Sat} is also visible with

an increase up to 182 emu.cm^{-3} for LSMO/NS/GS sample with the increase of T_G. The rise in the saturation magnetization is somewhat lower for the polycrystalline and the single-crystal LSMO films (63 and 35 emu.cm^{-3}, respectively). For LSMO/NS/GS samples, the magnetization is between the values measured on the two other samples at T_G=550°C but is similar to LSMO on (001)STO at T_G=645°C. This behavior confirms the enhancement of the structural quality of LSMO films provided by NS. The coercivity H_C is subjected to a similar behavior as function of the nature of the substrate. The lower value of H_C is observed for the LSMO films on STO with 27 and 52 × 10^{-4} T at T_G =550 and 645°C. Thus, H_C is divided by 2 as function of T_G. These low values of the coercivity reflect the single crystal structure and large magnetic domains. In contrast, the hysteresis loops suffer a spreading for LSMO/GS with values increasing up to ~350 and ~250 Oe for T_G = 550°C and 645°C. In the polycrystalline LSMO samples, the formation of magnetic domains is driven by the particle size influenced by the growth temperature. As suggested by Lecoeur *et al.*[56], the domains switch mostly independently each in a narrow range of fields and since the distribution of switching fields is large, it provides a higher macroscopic coercivity when the particle size decreases. For (001)-textured LSMO/NS/GS, the value of H_C decreases noticeably compared to polycrystalline LSMO/GS films. This change is consistent with the improvement of the structural quality and the particle size evidenced by AFM and XRD measurements for the textured films.

Nevertheless, the combination of shape and magnetocrystalline anisotropy in epitaxial (001)-oriented LSMO films induces a magnetic anisotropy along preferential crystallographic orientations which minimize the magnetostatic energy when an external field is applied[57]. As such, the [110] and [100] directions are identified to be easy and hard axes, respectively. When the magnetization change over from the [100] to the [110] axis, the hysteresis loop becomes larger and the coercivity increases. In polycrystalline films grown on glass, the full misorientation of grains leads to the statistical distribution of the easy and hard axis of the individual grains in all directions of space, and therefore to a random orientation in the macroscopic measurements. The shape anisotropy is no longer relevant and the more likely easy axis take place in the [111] axis of respective oriented grains[58,59], resulting in the weakening of the square-shape hysteresis loop. For (001)-textured LSMO/NS/GS films, both [110] and [100] orientations are randomly in-plane distributed leading to a more narrowed magnetic response.

Therefore, the presence of NS improves greatly the coercivity of LSMO films with respect to the polycrystalline films by inducing larger magnetic domains. The LSMO films undergo a magnetic transition from magnetically hard to a magnetically soft material as function of the substrate.

3.3. Transport properties

The temperature dependence of the electrical resistivity measured at 0 and 9 T is plotted in Figure 5, for T_G = 550°C (a) and 645°C (b). Contrary to magnetic measurements, the magnetic field applied in the PPMS system is perpendicular to the film surface. At first glance, the zero-field resistivity at 300 K of polycrystalline LSMO films grown on GS is always higher than the resistivity of films deposited on STO and NS/GS. The global difference in the resistivity level observed for polycrystalline LSMO/GS samples compared to LSMO on STO is explained by the effective incorporation of grain boundaries acting as a local blockage to the electron delocalization across the crystalline domains. This behavior can be correlated to our AFM and XRD structural characterizations for which a smaller grain size is observed in the case of the complete polycrystalline films grown on GS (see Table 1 for more details). However, the discrepancy is weaker between LSMO deposited on NS and STO, especially for T_G = 645°C. Hence, the improvement of the transport is explained by two independent contributions driven by the structural quality of films. First, the growth temperature leads to a better film crystallinity with larger crystalline domains. Secondly, NS enhance greatly the structural quality of short range-epitaxial LSMO films by inducing the high texturation along the [001] direction and an increase of the grains size with a different growth mechanism on the scale of NS. Therefore, the use of NS promotes the carriers delocalization and the lowering of the resistivity. Moreover, in the low temperature region below 50 K, a resistivity minimum appears for LSMO films grown on GS and NS/GS and not present for LSMO/STO one. The nature of this effect is *H*-dependent as evidenced by the resistivity minimum shift toward lower temperature and flattens out when a magnetic field of 9 T is applied (see Figure S10). This effect is related to the presence of grain boundaries which act as diffusion scattering for the transport carrier which are not present for film deposited onto single crystal substrates[60,61]. Numerous models based on the electronic localization have been proposed to explain the appearance of the resistivity minimum within

the low-temperature range observed in other manganites[61–65]. The first one is a Coulomb blockade effect related to weak localization and strong electron-electron interaction in a disordered metallic state. Localized charge carriers need to overcome the Coulomb barrier and the magnetic tunnel barrier to tunnel from a grain to the other. With the reduction of particle sizes, the contribution of the Coulomb barrier increases and leads to a steeper rise in resistivity. This effect is presumed to prevail for small grains (below 50 nm)[61].

The second model consists in the contribution of intergranular spin-polarized tunneling (ISPT) between antiferromagnetically coupled grains through the grain boundaries[63]. The transport across the grain boundaries is sensitive to the applied magnetic field. Under zero external *H*-field, the neighboring grains align in such a way that the charge carriers of the grains have opposite spins and remains immobile. Such anti-ferromagnetic interaction results in a gap between the charge carriers of the neighboring grains. With increasing temperature, the grains reorient themselves and the carriers have enough energy to overcome the barrier (resistance decreases). Application of external magnetic field forces the grains to orient such that the spins carrier from the neighboring grains aligns favorably to reduce the energy gap. According to this model, the resistivity minimum should flatten out gradually with increasing field and vanish at some critical field. In this way, the resistivity minimum is nearly suppressed at $H = 9$ T for the LSMO film grown at 645°C on NS/GS and largely reduced for other polycrystalline substrates (see Figure S10).

Another important part resulting from the transport curves in Figure 5 (a) and (b) is the maximum of resistivity identified as the metal-insulator transition (T_P) usually correlated to the magnetic transition from ferromagnetic–metal (FM-M) to paramagnetic–insulator (PM-I). This effect can also be seen on the minimum of magnetoresistance MR defined as $MR = 100 \times (\rho_0 - \rho_H)/\rho_0$, where ρ_0 is the zero-field resistivity and ρ_H is the resistivity in the applied field H is plotted versus the temperature dependence in Figure 5 (c) and (d).

LSMO films show T_P around the temperature range of 225–312 K for the different type of substrates (see Table 1 for more details). By comparing the difference in temperature between the magnetic and the electrical transition $\Delta T = T_C - T_P$, we observe a rise in the discrepancy between the two distinct transitions in polycrystalline films. The variation of ΔT is specifically more important at $T_G = 645$°C. In a perfect LSMO single crystal, the difference must stay near zero[13,66]. However, the existence of grain domains in LSMO films deposited on GS and a lesser extent, in LSMO films grown on NS/GS influences the transport mechanisms. The electrical transition in polycrystalline films is strongly dependent on the

percolation threshold between neighboring grains in such a way that conduction path have to be established to ensure the carrier delocalization. On the reverse, the magnetic transition is statistically dependent on the commutation of each domain, leading to an average contribution around the observed T_C. Finally, the magnetic transition is more influenced by the structural properties of films such as the crystallographic phase or strains modifications than the particle size. In consequence ΔT is more representative of the morphology of films. This effect is clearly highlighted here in Figure 5 (c) and (d) with the displacement of dash lines stand for the metal-insulator transition, leading to a lower apparent T_P for polycrystalline films. Therefore, the presence of NS on GS enhances the morphology of LSMO films (larger particle size and preferential orientation) and results in the displacement of the metal-insulator transition by stabilizing the metallic state at higher temperature.

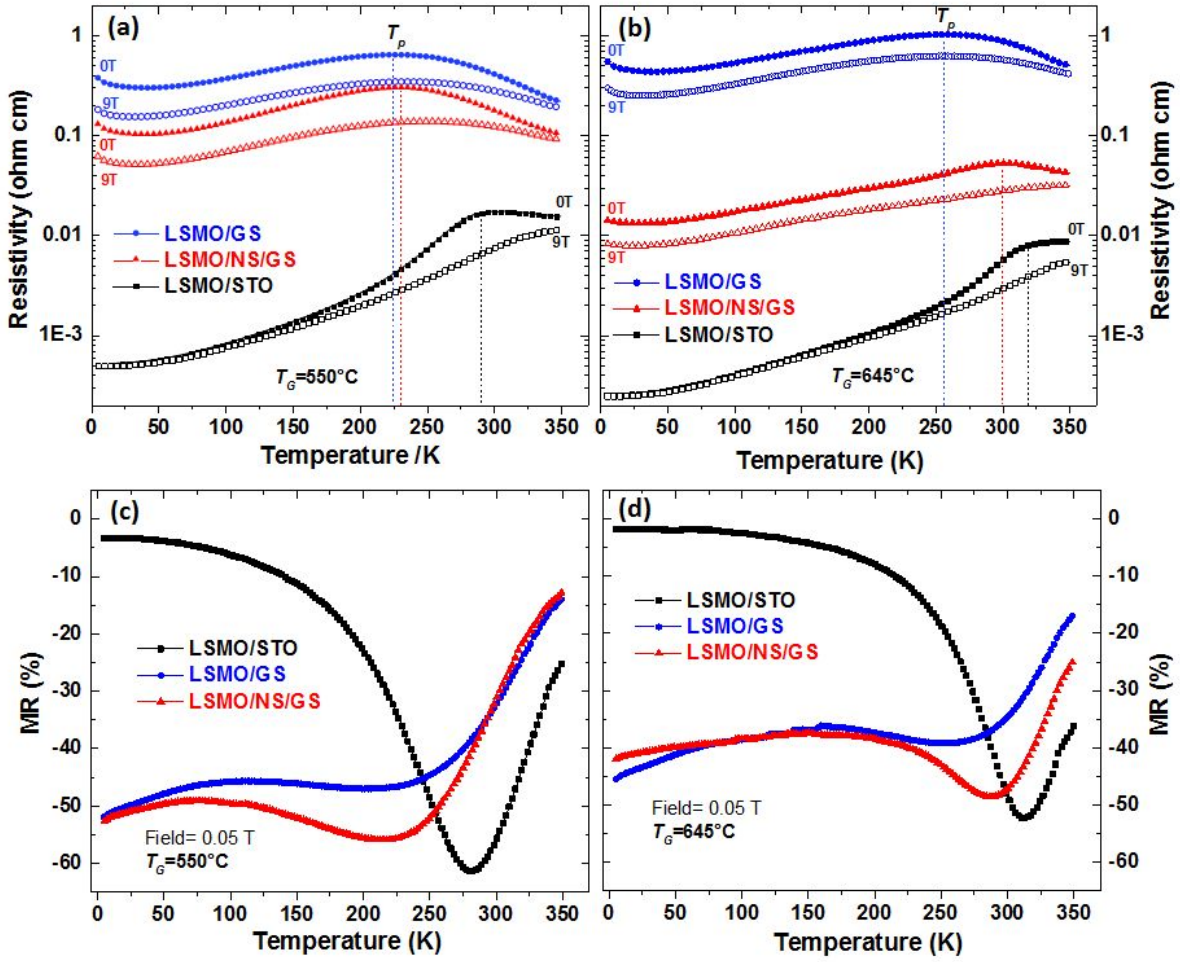

Figure 5. (a) Resistivity of LSMO films measured in parallel configuration at H = 0 T and 9 T for T_G = 550°C (a) and 645°C (b) and different substrates (STO, NS/GS, GS). (b)

Dependence of the magnetoresistance of films as function of the temperature at T_G = 550°C (c) and 645°C (d).

The amplitude of the MR is also very different with temperature depending on the different substrates (see Figures 5 (c) and (d)). In LSMO/STO samples, the low temperature MR is almost suppressed in good agreement with result reported by Yang *et al.* for single crystals substrates[67]. At the contrary, from low temperature to the apparent metal-insulator transition around 200 K, the MR of LSMO films on GS and NS/GS is constant with a value between 40 to 50%. Also, it is interesting to note that a strong MR is preserved within the low temperature range far below the transition for polycrystalline and textured films. In the case of textured LSMO films on NS/GS, this remarkable behavior represents of interest given that textured films have a high magnetization close to films of high quality deposited onto $SrTiO_3$. The presence of MR at low temperature for the textured LSMO film on NS is due to the grain boundaries of the textured polycrystalline structure. Furthermore, the presence of small polycrystalline domains on not covered GS zones confirmed by the presence of polycrystalline LSMO traces detected by XRD measurements (Figure 2) and AFM characterizations (Figure S2 (d)) can also amplify this low temperature MR.

To investigate deeper the transport response of films when a magnetic field is applied, we present in Figure 6 (a) and (b), the MR at 5 K versus *H*. For LSMO/STO samples, the MR is very weak, whereas LSMO/GS and LSMO/NS/GS samples show a high negative MR at 5 K of about –55 and –45 % for T_G = 550 and 645°C, respectively.

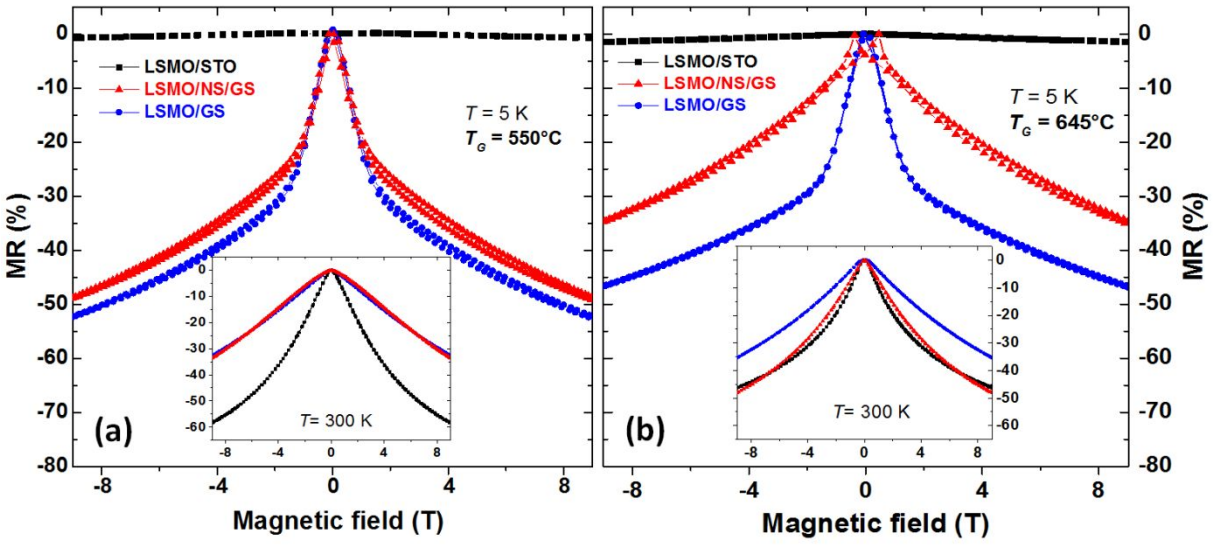

Figure 6. Magnetoresistance of LSMO films measured with magnetic field applied perpendicular to the surface at 5 K and 300 K (in insert), for T_G = 550°C (a) and 645°C (b) on STO (black), NS/GS (red) and GS (blue).

Interestingly, the MR increases rapidly in the low-field region. This behavior known as low-field effect is only observed for polycrystalline and textured LSMO films and is suppressed at 300 K (inset of Figure 6). The low-temperature MR in the polycrystalline films at low fields can be understood in terms of magnetic domain scattering at the boundary regions. Since the conduction electrons are almost completely polarized inside a magnetic domain, electrons are easily transferred between pairs of Mn^{3+} and Mn^{4+} ions[60,68]. However, when these electrons travel across grains, strong spin-dependent scattering at the boundaries will lead to a high zero-field resistivity. Application of a moderately low field can readily align the domains into a parallel configuration causing the resistivity to drop substantially. This phenomenon is very important for sensor applications[69] and we are showing the possibility to tune this behavior with the different type of substrate and temperature growth. This is particularly interesting because with the different type of substrate, we are able to stabilize highly-textured LSMO films deposited on CNO NS while limiting the resistivity threshold unlike pure polycrystalline films.

Table 1. Magnetic and electrical properties of LSMO films deposited on different substrates at 550 and 645°C.

Substrate	T_G [°C]	Grain size [nm]	T_C [K]	T_P [K]	$\Delta T = T_C - T_P$ [K]	M (0.05T) [emu cm^{-3}]	$\pm B_{Sat}$ [emu cm^{-3}]	$\pm H_c$ (100 K) [$\times 10^{-4}$ T]	ρ_{300K} (0Oe) [Ω cm]	CMR (300K) [%]	MR low field [%]
GS	550	14	333	227	106	256	278;–274	252;–255	2.7×10^{-1}	30	30
NS/GS	550	21	318	230	88	425	390;–422	248;–212	1.2×10^{-1}	35	20
STO	550	-	304	281	23	453	569;–575	23;–47	7.0×10^{-3}	60	–
GS	645	34	348	257	91	271	329;–331	357;–357	5.7×10^{-1}	35	30
NS/GS	645	40	337	300	37	443	581;–575	172;–173	2.8×10^{-2}	50	-
STO	645	-	332	312	20	463	596;–600	52;–52	2.9×10^{-3}	45	-

4. Conclusion

Chemical synthesis and deposition of homogeneous CNO NS layer on GS have been achieved with a coverage level close to 90%. Then, highly (001)-textured LSMO films on NS/GS have been grown with a high structural quality by taking advantage of randomly dispersed CNO NS used as seed layer. In contrast, LSMO on glass without NS result in fully polycrystalline films without any texturation, as confirmed by XRD and EBSD analyses. The preferential growth of LSMO on NS leads to magnetic and transport properties between the polycrystalline and single crystal LSMO ones used as reference in this work. As example, B_{sat} and increase by 250 emu cm^{-3} while T_C, H_C and ρ_{300K} are reduced by 10 K, 180 × 10^{-4} T and 5.67 × 10^{-4} Ω cm, respectively when the buffer NS seed layer is deposited on GS. Hence, the coercivity of the textured LSMO/NS/GS films is divided by 2 compared to LSMO on GS, thus allowing to switch between a hard magnetically ferromagnetic LSMO on glass to an easier magnetically tuning LSMO on NS. Finally, the magnetization and the coercivity of textured films are very close to the single crystal ones. A further advantage is that a low field MR appears for textured films, which is absent for single-crystalline films but present for polycrystalline films. Accordingly, structural and physical properties are widely improved by the use of NS in the case of the integration of LSMO on glass and combine the properties of monocrystalline and polycrystalline films.

Another notable advance is the possibility to preserve interesting physical properties of LSMO films grown at 550°C on NS/GS, which is not the case for polycrystalline films on GS. The reduction of the growth temperature opens new opportunities to integrate readily textured LSMO of high quality on silicon at lower temperature, without to consider the formation of native SiO_2. Also, the reduction of the temperature preserves more thermally sensitive substrates. In the near future, a fine adjustment of the coverage level of the surface by NS should also allow to tune the physical properties of deposited films on more complicated surfaces.

To summarize, $Ca_2Nb_3O_{10}^-$ nanosheets open new perspectives and opportunities for integration of perovskite structures like LSMO on various templates besides single crystal substrates. Thereby, diverse non-adapted substrates such as amorphous substrates (glass…) or crystalline substrates (silicon…) can be now considered while maintaining good structural and physical properties of films. This approach overcomes technological limitations for the use of complex oxides into CMOS-based applications.

Supporting Information

TEM brightfield micrograph of NS, AFM images, RHEED patterns, High-resolution θ-2θ diffractograms, X-Ray Reflectometry, SEM micrographs, Determination of Curie Temperature, Transport properties at low temperature

Acknowledgements

The authors thank the French Agence Nationale de la Recherche (ANR) (ANR-17-CE08-0012) in the framework of the POLYNASH project. TEM experiments were performed on THEMIS platform (ScanMAT, UMS 2011 University of Rennes 1-CNRS; CPER-FEDER 2007–2014). The authors thank L. Gouleuf and J. Lecourt for the substrate preparation and S. Gascoin for XRD characterizations.

References

(1) Zhang, G. Q.; Graef, M.; van Roosmalen, F. The Rationale and Paradigm of "More Than Moore"; *IEEE*, **2006**; 151–157.

(2) Kaur, J. Life Beyond Moore: More Moore or More Than Moore–A Review. *IJCSMC* **2016**, 5 (6), 233–237.

(3) Coey, J. M. D.; Viret, M.; von Molnár, S. Mixed-valence Manganites. *Advances in Physics* **1999**, *48* (2), 167–293.

(4) Salamon, M. B.; Jaime, M. The Physics of Manganites: Structure and Transport. *Reviews of Modern Physics* **2001**, *73* (3), 583–628.

(5) Boschker, H.; Huijben, M.; Vailionis, A.; Verbeeck, J.; van Aert, S.; Luysberg, M.; Bals, S.; van Tendeloo, G.; Houwman, E. P.; Koster, G.; Blank, D. H. A.; Rijnders, G. Optimized Fabrication of High-quality $La_{0.67}Sr_{0.33}MnO_3$ Thin Films Considering All Essential Characteristics. *Journal of Physics D: Applied Physics* **2011**, *44* (20), 205001.

(6) Fujishiro, H.; Ikebe, M.; Konno, Y.; Fukase, T. Sound Velocity Anomaly Associated with Polaron Ordering in $La_{1-x}Sr_xMnO_3$. *Journal of the Physical Society of Japan* **1997**, *66* (12), 3703–3705.

(7) Fujishiro, H.; Fukase, T.; Ikebe, M. Charge Ordering and Sound Velocity Anomaly in $La_{1-x}Sr_xMnO_3$ ($x \geq 0.5$). *Journal of the Physical Society of Japan* **1998**, *67* (8), 2582–2585.

(8) Huang, J.; Wang, H.; Sun, X.; Zhang, X.; Wang, H. Multifunctional $La_{0.67}Sr_{0.33}MnO_3$ (LSMO) Thin Films Integrated on Mica Substrates Toward Flexible Spintronics and Electronics. *ACS Applied Materials & Interfaces* **2018**, *10* (49), 42698–42705.

(9) Stankevič, V.; Šimkevičius, č.; Keršulis, S.; Balevičius, S.; Žurauskienė, N.; Pavilonis, D.; Tolvaišienė, S. Improvement in the Long-term Stability of Parameters of Encapsulated Magnetic Field Sensors Based on LaSrMnO Thin Films. *Sensors and Actuators A: Physical* **2015**, *228*, 112–117.

(10) Rousseau, O.; Flament, S.; Guillet, B.; Sing, M. L. C.; Méchin, L. Magnetic Sensors Based on AMR Effect in LSMO Thin Films. *Proceedings* **2017**, *1* (4), 635.
(11) Chappert, C.; Fert, A.; Van Dau, F. N. The Emergence of Spin Electronics in Data Storage. In *Nanoscience And Technology: A Collection of Reviews from Nature Journals*; World Scientific, **2010**; 147–157.
(12) Bibes, M.; Villegas, J. E.; Barthélémy, A. Ultrathin Oxide Films and Interfaces for Electronics and Spintronics. *Advances in Physics* **2011**, *60* (1), 5–84.
(13) Cesaria, M.; Caricato, A. P.; Maruccio, G.; Martino, M. LSMO – Growing Opportunities by PLD and Applications in Spintronics. *Journal of Physics: Conference Series* **2011**, *292*, 012003.
(14) Majumdar, S.; Dijken, S. van. Pulsed Laser Deposition of $La_{1-x}Sr_xMnO_3$: Thin-film Properties and Spintronic Applications. *Journal of Physics D: Applied Physics* **2014**, *47* (3), 034010.
(15) Sukhorukov, Y. P.; Moskvin, A. M.; Loshkareva, N. N.; Smolyak, I. B.; Arkhipov, V. E.; Mukovskii, Y. M.; Shmatok, A. V. Magnetooptical Faraday Effect in $La_{0.7}Sr_{0.3}MnO_{3-\delta}$ Films. *Technical Physics* **2001**, *46* (6), 778–781.
(16) Strutner, S. M.; Garcia, A.; Ula, S.; Adamo, C.; Richards, W. L.; Wang, K.; Schlom, D. G.; Carman, G. P. Index of Refraction Changes Under Magnetic Field Observed in $La_{0.66}Sr_{0.33}MnO_3$ Correlated to the Magnetorefractive Effect. *Optical Materials Express* **2017**, *7* (2), 468.
(17) Choi, Y.; Lynch, M. E.; Lin, M. C.; Liu, M. Prediction of O_2 Dissociation Kinetics on $LaMnO_3$-Based Cathode Materials for Solid Oxide Fuel Cells. *The Journal of Physical Chemistry C* **2009**, *113* (17), 7290–7297.
(18) Jalili, H.; Han, J. W.; Kuru, Y.; Cai, Z.; Yildiz, B. New Insights into the Strain Coupling to Surface Chemistry, Electronic Structure, and Reactivity of $La_{0.7}Sr_{0.3}MnO_3$. *The Journal of Physical Chemistry Letters* **2011**, *2* (7), 801–807.
(19) Hwang, H. Y.; Palstra, T. T. M.; Cheong, S.-W.; Batlogg, B. Pressure Effects on the Magnetoresistance in Doped Manganese Perovskites. *Physical Review B* **1995**, *52* (21), 15046–15049.
(20) Wang, C.; Jin, K.; Gu, L.; Lu, H.; Li, S.; Zhou, W.; Zhao, R.; Guo, H.; He, M.; Yang, G. Crucial Role Played by Interface and Oxygen Content in Magnetic Properties of Ultrathin Manganite Films. *Applied Physics Letters* **2013**, *102* (25), 252401.
(21) Picozzi, S.; Ma, C.; Yang, Z.; Bertacco, R.; Cantoni, M.; Cattoni, A.; Petti, D.; Brivio, S.; Ciccacci, F. Oxygen Vacancies and Induced Changes in the Electronic and Magnetic Structures of $La_{0.66}Sr_{0.33}MnO_3$: A Combined *Ab Initio* and Photoemission Study. *Physical Review B* **2007**, *75* (9).
(22) Li, F.; Zhan, Y.; Lee, T.-H.; Liu, X.; Chikamatsu, A.; Guo, T.-F.; Lin, H.-J.; Huang, J. C. A.; Fahlman, M. Modified Surface Electronic and Magnetic Properties of $La_{0.6}Sr_{0.4}MnO_3$ Thin Films for Spintronics Applications. *The Journal of Physical Chemistry C* **2011**, *115* (34), 16947–16953.
(23) Vailionis, A.; Boschker, H.; Siemons, W.; Houwman, E. P.; Blank, D. H. A.; Rijnders, G.; Koster, G. Misfit Strain Accommodation in Epitaxial ABO_3 Perovskites: Lattice Rotations and Lattice Modulations. *Physical Review B* **2011**, *83* (6).
(24) Nori, R.; Kale, S. N.; Ganguly, U.; Ravi Chandra Raju, N.; Sutar, D. S.; Pinto, R.; Ramgopal Rao, V. Morphology and Curie Temperature Engineering in Crystalline $La_{0.7}Sr_{0.3}MnO_3$ Films on Si by Pulsed Laser Deposition. *Journal of Applied Physics* **2014**, *115* (3), 033518.
(25) Mercey, B.; David, A.; Copie, O.; Prellier, W. Monitoring the Growth of $SrTiO_3$ and $La_{0.66}Sr_{0.33}MnO_3$ Thin Films Using a Low-pressure Reflection High Energy Electron Diffraction System. *Physica B: Condensed Matter* **2016**, *503*, 100–105.

(26) Neergaard Waltenburg, H.; Yates, J. T. Surface Chemistry of Silicon. *Chemical Reviews* **1995**, *95* (5), 1589–1673.
(27) Seo, J. W.; Fompeyrine, J.; Guiller, A.; Norga, G.; Marchiori, C.; Siegwart, H.; Locquet, J.-P. Interface Formation and Defect Structures in Epitaxial $La_2Zr_2O_7$ Thin Films on (111) Si. *Applied Physics Letters* **2003**, *83* (25), 5211–5213.
(28) Fontcuberta, J.; Bibes, M.; Martínez, B.; Trtik, V.; Ferrater, C.; Sánchez, F.; Varela, M. Tunable Epitaxial Growth of Magnetoresistive $La_{2/3}Sr_{1/3}MnO_3$ Thin Films. *Journal of Applied Physics* **1999**, *85* (8), 4800–4802.
(29) Perna, P.; Méchin, L.; Chauvat, M. P.; Ruterana, P.; Simon, C.; Scotti di Uccio, U. High Curie Temperature for $La_{0.7}Sr_{0.3}MnO_3$ Thin Films Deposited on CeO_2/YSZ-based Buffered Silicon Substrates. *Journal of Physics: Condensed Matter* **2009**, *21* (30), 306005.
(30) Groenen, R.; Liao, Z.; Gauquelin, N.; Hoekstra, R.; Spanjer, B.; van Gorsel, M.; Borkent, S.; Nguyen, M.; Vargas-LLona, L.; Rodijk, E. Epitaxial Growth of Complex Oxides on Silicon by Enhanced Surface Diffusion in Large Area Pulsed Laser Deposition. *arXiv preprint arXiv:1607.05955* **2016**.
(31) Tiwari, A.; Chug, A.; Jin, C.; Kumar, D.; Narayan, J. Integration of Single Crystal $La_{0.7}Sr_{0.3}MnO_3$ Films with Si(001). *Solid State Communications* **2002**, *121* (12), 679–682.
(32) Belmeguenai, M.; Mercone, S.; Adamo, C.; Chauveau, T.; Méchin, L.; Monod, P.; Moch, P.; Schlom, D. G. $La_{0.7}Sr_{0.3}MnO_3$ Thin Films on $SrTiO_3$ and $CaTiO_3$ Buffered Si Substrates: Structural, Static, and Dynamic Magnetic Properties. *Journal of Nanoparticle Research* **2011**, *13* (11), 5669–5675.
(33) Méchin, L.; Adamo, C.; Wu, S.; Guillet, B.; Lebargy, S.; Fur, C.; Routoure, J.-M.; Mercone, S.; Belmeguenai, M.; Schlom, D. G. Epitaxial $La_{0.7}Sr_{0.3}MnO_3$ Thin Films Grown on $SrTiO_3$ Buffered Silicon Substrates by Reactive Molecular-beam Epitaxy. *Physica Status Solidi (a)* **2012**, *209* (6), 1090–1095.
(34) Huang, J.; Gellatly, A.; Kauffmann, A.; Sun, X.; Wang, H. Exchange Bias Effect Along Vertical Interfaces in $La_{0.7}Sr_{0.3}MnO_3$:NiO Vertically Aligned Nanocomposite Thin Films Integrated on Silicon Substrates. *Crystal Growth & Design* **2018**, *18* (8), 4388–4394.
(35) Nijland, M.; Thomas, S.; Smithers, M. A.; Banerjee, N.; Blank, D. H. A.; Rijnders, G.; Xia, J.; Koster, G.; ten Elshof, J. E. Epitaxy on Demand. *Advanced Functional Materials* **2015**, *25* (32), 5140–5148.
(36) Yuan, H.; Lubbers, R.; Besselink, R.; Nijland, M.; ten Elshof, J. E. Improved Langmuir–Blodgett Titanate Films via in Situ Exfoliation Study and Optimization of Deposition Parameters. *ACS Applied Materials & Interfaces* **2014**, *6* (11), 8567–8574.
(37) Li, B.-W.; Osada, M.; Ebina, Y.; Akatsuka, K.; Fukuda, K.; Sasaki, T. High Thermal Robustness of Molecularly Thin Perovskite Nanosheets and Implications for Superior Dielectric Properties. *ACS Nano* **2014**, *8* (6), 5449–5461.
(38) Shibata, T.; Ebina, Y.; Ohnishi, T.; Takada, K.; Kogure, T.; Sasaki, T. Fabrication of Anatase Thin Film with Perfect *c*-Axis Orientation on Glass Substrate Promoted by a Two-Dimensional Perovskite Nanosheet Seed Layer. *Crystal Growth & Design* **2010**, *10* (8), 3787–3793.
(39) Kimura, J.; Takuwa, I.; Matsushima, M.; Shimizu, T.; Uchida, H.; Kiguchi, T.; Shiraishi, T.; Konno, T. J.; Shibata, T.; Osada, M.; Sasaki, T.; Funakubo, H. Thermally Stable Dielectric Responses in Uniaxially (001)-oriented $CaBi_4Ti_4O_{15}$ Nanofilms Grown on a $Ca_2Nb_3O_{10}^-$ Nanosheet Seed Layer. *Scientific Reports* **2016**, *6* (1).

(40) Kweon, S.-H.; Im, M.; Lee, W.-H.; Nahm, S.; Choi, J.-W.; Hwang, S.-J. Electrophoretic Deposition of $Ca_2Nb_3O_{10}^-$ Nanosheets Synthesized by Soft-chemical Exfoliation. *Journal of Materials Chemistry C* **2016**, *4* (1), 178–184.
(41) Shibata, T.; Takano, H.; Ebina, Y.; Kim, D. S.; Ozawa, T. C.; Akatsuka, K.; Ohnishi, T.; Takada, K.; Kogure, T.; Sasaki, T. Versatile van Der Waals Epitaxy-like Growth of Crystal Films Using Two-dimensional Nanosheets as a Seed Layer: Orientation Tuning of $SrTiO_3$ Films Along Three Important Axes on Glass Substrates. *J. Mater. Chem. C* **2014**, *2* (3), 441–449.
(42) Nijland, M.; Kumar, S.; Lubbers, R.; Blank, D. H. A.; Rijnders, G.; Koster, G.; ten Elshof, J. E. Local Control over Nucleation of Epitaxial Thin Films by Seed Layers of Inorganic Nanosheets. *ACS Applied Materials & Interfaces* **2014**, *6* (4), 2777–2785.
(43) Dion, M.; Ganne, M.; Tournoux, M. Nouvelles Familles de Phases $MIMII_2Nb_3O_{10}$ a Feuillets "perovskites". *Materials Research Bulletin* **1981**, *16* (11), 1429–1435.
(44) Tokumitsu, T.; Toda, K.; Aoyagi, T.; Sakuraba, D.; Uematsu, K.; Sato, M. Powder Neutron Diffraction Study of Layered Perovskite, $KCa_2Nb_3O_{10}$. *Journal of the Ceramic Society of Japan* **2006**, *114* (1333), 795–797.
(45) Lepetit, M.-B.; Mercey, B.; Simon, C. Interface Effects in Perovskite Thin Films. *Physical Review Letters* **2012**, *108* (8), 087202.
(46) Fang, S.; Pang, Z.; Wang, F.; Lin, L.; Han, S. Annealing Effect on Transport and Magnetic Properties of $La_{0.67}Sr_{0.33}MnO_3$ Thin Films Grown on Glass Substrates by RF Magnetron Sputtering. *Journal of Materials Science & Technology* **2011**, *27* (3), 223–226.
(47) Ebina, Y.; Akatsuka, K.; Fukuda, K.; Sasaki, T. Synthesis and In Situ X-ray Diffraction Characterization of Two-Dimensional Perovskite-Type Oxide Colloids with a Controlled Molecular Thickness. *Chemistry of Materials* **2012**, *24* (21), 4201–4208.
(48) Nguyen, M. D.; Houwman, E. P.; Yuan, H.; Wylie-van Eerd, B. J.; Dekkers, M.; Koster, G.; ten Elshof, J. E.; Rijnders, G. Controlling Piezoelectric Responses in $Pb(Zr_{0.52}Ti_{0.48})O_3$ Films through Deposition Conditions and Nanosheet Buffer Layers on Glass. *ACS Applied Materials & Interfaces* **2017**, *9* (41), 35947–35957.
(49) Navasery, M.; Halim, S. A.; Soltani, N.; Bahmanrokh, G.; Erfani, M.; Chen, S. K.; Lim, K. P.; Awang Kechik, M. M. Growth and Characterization of $La_{5/8}Sr_{3/8}MnO_3$ Thin Films Prepared by Pulsed Laser Deposition on Different Substrates. *Journal of Materials Science: Materials in Electronics* **2014**, *25* (3), 1317–1324.
(50) Hibble, S. J.; Cooper, S. P.; Hannon, A. C.; Fawcett, I. D.; Greenblatt, M. Local Distortions in the Colossal Magnetoresistive Manganates $La_{0.70}Ca_{0.30}MnO_3$, $La_{0.80}Ca_{0.20}MnO_3$ and $La_{0.70}Sr_{0.30}MnO_3$ Revealed by Total Neutron Diffraction. *Journal of Physics: Condensed Matter* **1999**, *11* (47), 9221–9238.
(51) Xu, F. F.; Ebina, Y.; Bando, Y.; Sasaki, T. Structural Characterization of (TBA, H)$Ca_2Nb_3O_{10}$ Nanosheets Formed by Delamination of a Precursor-Layered Perovskite. *The Journal of Physical Chemistry B* **2003**, *107* (36), 9638–9645.
(52) Klug, H. P. *X-ray Diffraction Procedures for Polycrystalline and Amorphous Materials*, 2d ed.; Wiley: New York, **1974**.
(53) Huijben, M.; Martin, L. W.; Chu, Y.-H.; Holcomb, M. B.; Yu, P.; Rijnders, G.; Blank, D. H. A.; Ramesh, R. Critical Thickness and Orbital Ordering in Ultrathin $La_{0.7}Sr_{0.3}MnO_3$ Films. *Physical Review B* **2008**, *78* (9).
(54) Kwon, C.; Robson, M. C.; Kim, K.-C.; Gu, J. Y.; Lofland, S. E.; Bhagat, S. M.; Trajanovic, Z.; Rajeswari, M.; Venkatesan, T.; Kratz, A. R. Stress-induced Effects in Epitaxial $(La_{0.7}Sr_{0.3})MnO_3$ Films. *Journal of Magnetism and Magnetic Materials* **1997**, *172* (3), 229–236.

(55) Tsui, F.; Smoak, M. C.; Nath, T. K.; Eom, C. B. Strain-dependent Magnetic Phase Diagram of Epitaxial $La_{0.67}Sr_{0.33}MnO_3$ Thin Films. *Applied Physics Letters* **2000**, *76* (17), 2421–2423.

(56) Lecoeur, P.; Trouilloud, P. L.; Xiao, G.; Gupta, A.; Gong, G. Q.; Li, X. W. Magnetic Domain Structures of $La_{0.67}Sr_{0.33}MnO_3$ Thin Films with Different Morphologies. *Journal of Applied Physics* **1997**, *82* (8), 3934–3939.

(57) Steenbeck, K.; Habisreuther, T.; Dubourdieu, C.; Sénateur, J. P. Magnetic Anisotropy of Ferromagnetic $La_{0.7}Sr_{0.3}MnO_3$ Epitaxial Thin Films: Dependence on Temperature and Film Thickness. *Applied Physics Letters* **2002**, *80* (18), 3361–3363.

(58) Urushibara, A.; Moritomo, Y.; Arima, T.; Asamitsu, A.; Kido, G.; Tokura, Y. Insulator-metal Transition and Giant Magnetoresistance in $La_{1-x}Sr_xMnO_3$. *Physical Review B* **1995**, *51* (20), 14103–14109.

(59) Konoto, M.; Kohashi, T.; Koike, K.; Arima, T.; Kaneko, Y.; Tomioka, Y.; Tokura, Y. Magnetic Domain Structure of a $La_{0.7}Sr_{0.3}MnO_3$ (001) Surface Observed by a Spin-polarized Scanning Electron Microscope. *Applied Physics Letters* **2004**, *84* (13), 2361–2363.

(60) Gupta, A.; Gong, G. Q.; Xiao, G.; Duncombe, P. R.; Lecoeur, P.; Trouilloud, P.; Wang, Y. Y.; Dravid, V. P.; Sun, J. Z. Grain-boundary Effects on the Magnetoresistance Properties of Perovskite Manganite Films. *Physical Review B* **1996**, *54* (22), R15629.

(61) Zhou, Y.; Zhu, X.; Li, S. Effect of Particle Size on Magnetic and Electric Transport Properties of $La_{0.67}Sr_{0.33}MnO_3$ Coatings. *Physical Chemistry Chemical Physics* **2015**, *17* (46), 31161–31169.

(62) Tomioka, Y.; Asamitsu, A.; Moritomo, Y.; Kuwahara, H.; Tokura, Y. Collapse of a Charge-ordered State Under a Magnetic Field in $Pr_{1/2}Sr_{1/2}MnO_3$. *Physical Review Letters* **1995**, *74* (25), 5108–5111.

(63) Battabyal, M.; Dey, T. K. Electrical Conductivity in $La_{1-x}Ag_xMnO_3$ Pellets Between 10 and 350 K. *Physica B: Condensed Matter* **2005**, *367* (1-4), 40–47.

(64) Petrov, D. K.; Krusin-Elbaum, L.; Sun, J. Z.; Feild, C.; Duncombe, P. R. Enhanced Magnetoresistance in Sintered Granular Manganite/insulator Systems. *Applied Physics Letters* **1999**, *75* (7), 995–997.

(65) Rozenberg, E.; Auslender, M.; Felner, I.; Gorodetsky, G. Low-temperature Resistivity Minimum in Ceramic Manganites. *Journal of Applied Physics* **2000**, *88* (5), 2578–2582.

(66) Ramirez, A. P. Colossal Magnetoresistance. *Journal of Physics: Condensed Matter* **1997**, *9* (39), 8171–8199.

(67) Yang, S. Y.; Kuang, W. L.; Liou, Y.; Tse, W. S.; Lee, S. F.; Yao, Y. D. Growth and Characterization of $La_{0.7}Sr_{0.3}MnO_3$ Films on Various Substrates. *Journal of Magnetism and Magnetic Materials* **2004**, *268* (3), 326–331.

(68) Hwang, H. Y.; Cheong, S.-W.; Ong, N. P.; Batlogg, B. Spin-Polarized Intergrain Tunneling in $La_{2/3}Sr_{1/3}MnO_3$. *Physical Review Letters* **1996**, *77* (10), 2041–2044.

(69) Xu, Y.; Memmert, U.; Hartmann, U. Magnetic Field Sensors from Polycrystalline Manganites. *Sensors and Actuators A: Physical* **2001**, *91* (1-2), 26–29.

For Table of Contents only: